

RL-TR-95-243
Final Technical Report
November 1995



FABRY-PEROT PHOTOREFRACTIVE QUANTUM WELL STRUCTURES FOR ADAPTIVE PROCESSING

Purdue University

David D. Nolte and M.R. Melloch

DTIC QUALITY INSPECTED 4

19960212 030

APPROVED FOR PUBLIC RELEASE; DISTRIBUTION UNLIMITED.

Rome Laboratory
Air Force Materiel Command
Rome, New York

This report has been reviewed by the Rome Laboratory Public Affairs Office (PA) and is releasable to the National Technical Information Service (NTIS). At NTIS, it will be releasable to the general public, including foreign nations.

RL-TR-95- 243 has been reviewed and is approved for publication.

APPROVED: *George Brost*

GEORGE BROST
Project Engineer

FOR THE COMMANDER: *Gary D. Barmore*

GARY D. BARMORE, Major, USAF
Deputy Director of Surveillance & Photonics

If your address has changed or if you wish to be removed from the Rome Laboratory mailing list, or if the addressee is no longer employed by your organization, please notify Rome Laboratory/ (OCPA), Rome NY 13441. This will assist us in maintaining a current mailing list.

Do not return copies of this report unless contractual obligations or notices on a specific document require that it be returned.

REPORT DOCUMENTATION PAGE

Form Approved
OMB No. 0704-0188

Public reporting burden for this collection of information is estimated to average 1 hour per response, including the time for reviewing instructions, searching existing data sources, gathering and maintaining the data needed, and completing and reviewing the collection of information. Send comments regarding this burden estimate or any other aspect of this collection of information, including suggestions for reducing this burden, to Washington Headquarters Services, Directorate for Information Operations and Reports, 1215 Jefferson Davis Highway, Suite 1204, Arlington, VA 22202-4302, and to the Office of Management and Budget, Paperwork Reduction Project (0704-0188), Washington, DC 20503.

1. AGENCY USE ONLY (Leave Blank)		2. REPORT DATE November 1995		3. REPORT TYPE AND DATES COVERED Final Feb 94 - Feb 95	
4. TITLE AND SUBTITLE FABRY-PEROT PHOTOREFRACTIVE QUANTUM WELL STRUCTURES FOR ADAPTIVE PROCESSING				5. FUNDING NUMBERS C - F30602-94-C-0002 PE - 62702F PR - 4600 TA - P1 WU - PT	
6. AUTHOR(S) David D. Nolte and M.R. Melloch					
7. PERFORMING ORGANIZATION NAME(S) AND ADDRESS(ES) Purdue University Department of Physics West Lafayette IN 47907				8. PERFORMING ORGANIZATION REPORT NUMBER N/A	
9. SPONSORING/MONITORING AGENCY NAME(S) AND ADDRESS(ES) Rome Laboratory/OCPA 25 Electronic Pky Rome NY 13441-4515				10. SPONSORING/MONITORING AGENCY REPORT NUMBER RL-TR-95-243	
11. SUPPLEMENTARY NOTES Rome Laboratory Project Engineer: George A. Brost/OCPA/(315) 330-7669					
12a. DISTRIBUTION/AVAILABILITY STATEMENT Approved for public release; distribution unlimited.				12b. DISTRIBUTION CODE	
13. ABSTRACT (Maximum 200 words) Photorefractive quantum well structures that use Fabry-Perot interference effects to enhance reflected diffraction were investigated numerically and experimentally. Hybrid transmission/reflection and fully asymmetric Fabry-Perot transverse field geometry and fully asymmetric Fabry-Perot longitudinal field geometry devices were studied. Diffraction was significantly enhanced by the Fabry-Perot resonance. The largest output diffraction efficiency of nearly 200% was achieved in a low temperature grown AlAs barrier multiple quantum well.					
14. SUBJECT TERMS Photorefraction, Fabry-Perot, Multiple quantum well				15. NUMBER OF PAGES 36	
				16. PRICE CODE	
17. SECURITY CLASSIFICATION OF REPORT UNCLASSIFIED	18. SECURITY CLASSIFICATION OF THIS PAGE UNCLASSIFIED	19. SECURITY CLASSIFICATION OF ABSTRACT UNCLASSIFIED	20. LIMITATION OF ABSTRACT UL		

Table of Contents

1. Introduction.....	3
2. Theory of operation.....	3
A. Photorefractive Grating Formation.....	3
B. Asymmetric Fabry-Perot Modulators.....	4
C. Diffraction in Asymmetric Fabry-Perots.....	5
3. Device Geometries.....	6
4. Theoretical Results.....	7
A. Transverse-Field geometry.....	7
1. Hybrid Transmission/Reflection Device.....	7
2. Fully Asymmetric Fabry-Perot.....	12
B. Longitudinal-Field geometry.....	13
5. Experimental Results.....	14
A. Hybrid Device.....	14
B. Fully Asymmetric Fabry-Perot.....	20
6. Discussion and Future Work.....	26
7. Bibliography.....	28

1. Introduction

Dynamic holography in a photorefractive asymmetric Fabry-Perot (ASFP) multiple quantum well (MQW) modulator has possible applications in adaptive signal processors [1]. Photorefractive MQWs have the advantages of working at low incident light intensities and at faster speeds than bulk photorefractive materials. Operating in transmission they have one of the largest dynamic diffraction efficiencies per interaction length of known optical materials [2, 3, 4]. However, the device diffraction efficiencies, which are limited by the trade-off between device absorption and electroabsorption, have not exceeded 3%, even when neglecting insertion loss and absorption [5].

Quantum well electroabsorption modulators benefit from larger absorption at the exciton transitions which produces larger electroabsorption and stronger gratings, but it also reduces the interaction length. This design bottleneck can partly be avoided by operating the photorefractive quantum-wells in reflection as asymmetric Fabry-Pérot (ASFP) structures. Quantum-well ASFP modulators have generated the largest contrast ratios in quantum-well structures by utilizing multiple beam interference [6]. In addition, the multiple beam interference is extremely sensitive to phase, making it possible to operate the ASFP as a phase modulator [7]. Phase gratings [8] are the most efficient means to diffract light. Careful placement of the Fabry-Perot fringes can yield an order of magnitude enhancement in the diffraction efficiency of the photorefractive MQW.

2. Theory of Operation

A. Photorefractive Grating Formation

Photorefractive devices operate as a result of changes in optical properties due to illumination by spatially varying light. The interference of two beams of light on a photorefractive material generates a spatially varying excitation of carriers which drift under an applied electric field. The separated charges are then trapped by defects, forming space-charge electric fields. Through the electro-optic effect the spatially varying electric field causes a spatial modulation of the refractive index of the material. Absorptive electro-optic effects cause an accompanying absorption modulation. Quantum confinement of excitons in the quantum wells yields large electro-optic effects which boosts diffractive performance over that of bulk semiconductor crystals [9]. Dynamic diffraction then occurs when a probe beam illuminates the gratings.

B. Asymmetric Fabry-Perot Modulator

Asymmetric Fabry-Perot quantum-well modulators take advantage of dual absorption and cavity resonances in a thin semiconductor film to balance the intensities reflected from the front face of the film and from a high reflector in back of the film. Asymmetric Fabry-Perot structures have been incorporated into the design of electro-optic modulators [10] and self electro-optic devices (SEEDs) [11] to increase the effective interaction length and to provide large on/off contrast ratios [12]. The basic structure of an ASFP is shown in Figure 2.1. (2)

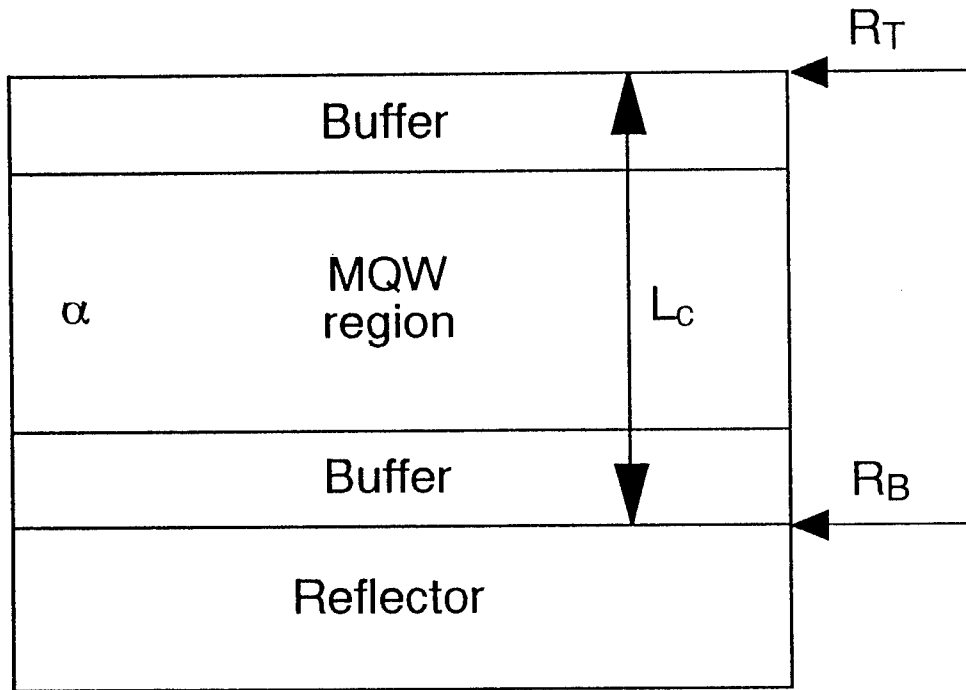


Figure 2.1. Basic structure of an ASFP modulator. A multiple quantum well layer is sandwiched between two optically inert buffers which control the center wavelength of the Fabry-Perot fringes.

The total reflectivity of the Fabry-Perot, R_{FP} is given by

$$R_{FP} = \frac{|\sqrt{R_T} - \sqrt{R_B} e^{-\alpha L_c}|^2}{|1 - \sqrt{R_T R_B} e^{-\alpha L_c}|^2} \quad (1)$$

where R_T is the front interface reflectivity, R_B is the back interface reflectivity, α is the absorption, and L_c is the cavity thickness. The cavity absorption balances the reflectivities from the front and back interfaces when $R_B < R_T$. Most importantly, $R_{FP} = 0$ when

$$R_B e(-2\alpha L_c) = R_T$$

The advantage of the Fabry-Perot modulator over absorption modulators [13] is the π phase difference between the reflected waves off the front and back interfaces which can yield a net reflectivity of exactly zero.

C. Diffraction in Asymmetric Fabry-Perots

Diffraction from thin film Fabry-Perots occurs in the Raman-Nath limit since the cavity length is short, typically 1-2 μm , and the grating period, typically 20-30 μm , is much longer than the cavity length. As a result, the Bragg condition does not need to be satisfied and the diffraction angles may be small. Integration of the signal over a single grating period for transmission is

$$E_t^d = \frac{1}{\Lambda} \int_0^\Lambda |E_t(x)| \exp[i\phi_t(x) - iMKx] dx \quad (3)$$

and for reflection is

$$E_r^d = \frac{1}{\Lambda} \int_0^\Lambda |E_r(x)| \exp[i\phi_r(x) - iMKx] dx \quad (4)$$

which yield the diffracted amplitudes in the Fraunhofer approximation.

Multiple beam interference within the cavity provides sensitive amplitude and phase control of the incident light. The reflected and transmitted field amplitudes from multiple layers are given by [14]

$$\begin{pmatrix} 1 \\ E_r \end{pmatrix} = \frac{C_1 C_2 \dots C_{n+1}}{t_1 t_2 \dots t_{n+1}} \begin{pmatrix} E_t \\ 0 \end{pmatrix} \quad (5)$$

where the C_m 's are the Fresnel matrices for each interface

$$C_m = \begin{pmatrix} \exp(i\delta_{m-1}) & r_m \exp(i\delta_{m-1}) \\ r_m \exp(-i\delta_{m-1}) & \exp(-i\delta_{m-1}) \end{pmatrix} \quad (6)$$

The m th Fresnel reflection coefficient, r_m , and m th phase, δ_m , are given by

$$r_m = \frac{n_{m-1} - n_m + i(\kappa_m - \kappa_{m-1})}{n_{m-1} + n_m + i(\kappa_m + \kappa_{m-1})} \quad (7)$$

and

$$\delta_m = \frac{2\pi}{\lambda} n_m \sum_{j=1}^{m-1} d_j \quad (8)$$

where d_j is the thickness of the j th layer. If the matrix product for the n layers is written as

$$C_1 C_2 \dots C_{n+1} = \begin{pmatrix} a & b \\ c & d \end{pmatrix} \quad (9)$$

the field amplitudes E_r and E_t used in (3) and (4) are given by

$$E_r = \frac{c}{a} \quad E_t = \frac{t_1 t_2 \dots t_{n+1}}{a} \quad (10)$$

3. Device Geometries

Several different device geometries exist for the diffractive ASFP. The two electric field geometries are the transverse-field geometry, in which the field broadening [15] of the exciton transition provides the electroabsorption necessary to balance the ASFP, and the longitudinal-field geometry, in which the electroabsorption is provided by the quantum-confined Stark effect [16]. In the transverse-field geometry the electric field is applied parallel to the quantum wells while in the longitudinal geometry the field is

applied perpendicular to the quantum wells. At low electric field strengths of 10^4 V/cm, the transverse electro-optic effect is stronger than the quantum-confined Stark effect (QCSE), although the QCSE is stronger at larger fields.

There are also two geometries which differ from each other in the ratio of their front and back interface reflectivities. When the MQW is bonded to glass, a hybrid device, or nearly-symmetric Fabry-Perot, is created. When operated with the light incident on the glass side, the glass-semiconductor interface is approximately 16% and the semiconductor-air interface is 31%. The advantage to the hybrid device is simultaneous operation in both transmission and reflection. The second reflection geometry is the fully asymmetric Fabry-Perot. The front interface is the air-semiconductor interface ($R = 31\%$) and the back interface consists of a high reflector ($R > 95\%$).

4. Numerical Results

A. Transverse-Field Geometry

1. Hybrid Transmission/Reflection Device

The partially asymmetric Fabry Perot device design is based on the transverse-transmission geometry of photorefractive quantum wells [4]. This design is particularly simple to fabricate and operate. It consists of a single layer of multiple quantum wells with a total thickness of approximately 2 microns. Electrodes are placed on the top surface of the quantum well layer and a voltage is applied parallel to the quantum-well planes. In this electric-field configuration the relevant electro-optic effect needed in the photorefractive process is the transverse-field Franz Keldysh effect, which is the field-broadening of the quantum-confined excitonic transition. This electro-optic effect is an electroabsorption process in which the excitonic absorption is changed by electric fields. Refractive index changes accompany the absorption changes through the Kramers-Kronig relations. Therefore both absorption as well as index gratings are present during holographic mixing between two coherent laser beams.

The quantum wells are fabricated as partially asymmetric Fabry-Perots by adhering one side of the free-standing quantum well structure to glass with a refractive index of approximately 1.5. This glass-semiconductor interface has a lower reflectivity than the semiconductor-air interface. This reflectivity, combined with the intrinsic absorption within the semiconductor, makes it possible for a light beam incident from the

glass side to satisfy an antireflection condition. The experimental configuration is shown in Fig. 4.1. The read beam experiences multiple beam interference for both transmission and reflection because of partial reflections from the glass-semiconductor and the semiconductor-air interfaces. The total transmitted and reflected intensities for such a structure with the read beam incident from the glass interface are simulated in Fig. 4.2. Details of the simulation program, which have full Kramers-Kronig transforms to accurately include spectral variation in the refractive index, are given in Ref [17]. The reflected intensity vanishes on the long-wavelength side of the excitonic transition. For longer wavelengths, additional Fabry Perot fringes are clearly visible. The transmitted intensity also shows strong interference fringes, but does not vanish for any wavelength. In this structure, the reflected intensity will therefore have large contrast ratios without the need of a high-reflectivity dielectric layer as in fully asymmetric Fabry-Perots.

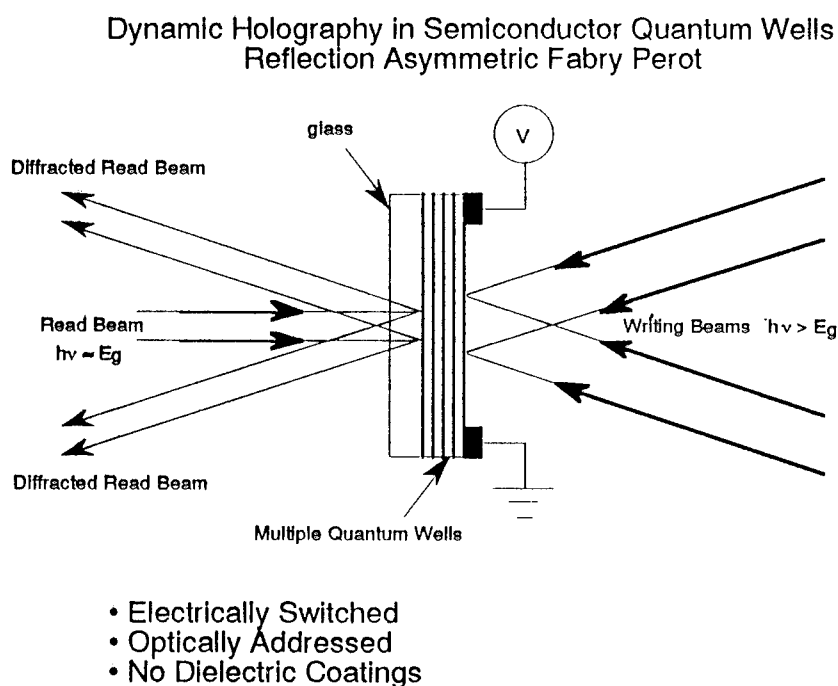


Fig. 4.1 Partially asymmetric Fabry-Perot device structure and operation. The read beam must be incident on the glass-semiconductor interface to have the mismatch of interface reflections balanced by the intrinsic quantum well absorption. Electrodes on the surface of the multiple quantum well layer induce photorefractive gratings in the device when two coherent writing beams produce interference fringes in the device

The device design and the optical implementation of the device as a holographic optical element (HOE) are shown in Fig. 4.1. The writing beams that form the interference patterns can have any photon energy larger than the bandgap of the quantum

well structure. These interference fringes are turned into absorption and index gratings through the photorefractive process. To read the gratings written in the quantum wells, a read laser beam (with a laser wavelength tuned close to the exciton transition wavelength) interrogates the gratings and is diffracted into multiple diffraction orders. In the system design shown in the figure, the probe laser can be incident with normal incidence from the side opposite to the writing laser beams, similar to the configuration of a light valve or incoherent-to-coherent converter.

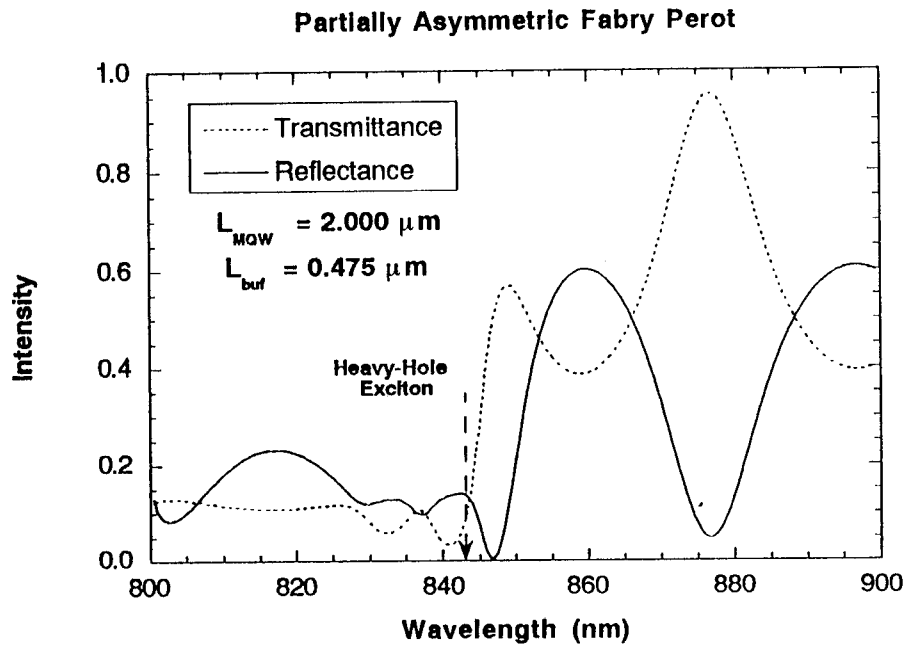


Fig. 4.2 Simulated reflectance and transmittance of a partially asymmetric Fabry Perot. The Fabry Perot fringe satisfies an antireflection condition on the long-wavelength side of the heavy-hole exciton transition wavelength.

In the case of the partially asymmetric Fabry-Perot, the first and last reflection coefficients are defined by the glass-semiconductor interface and by the semiconductor-air interface. The difference between these reflection coefficients is balanced by the internal absorption.

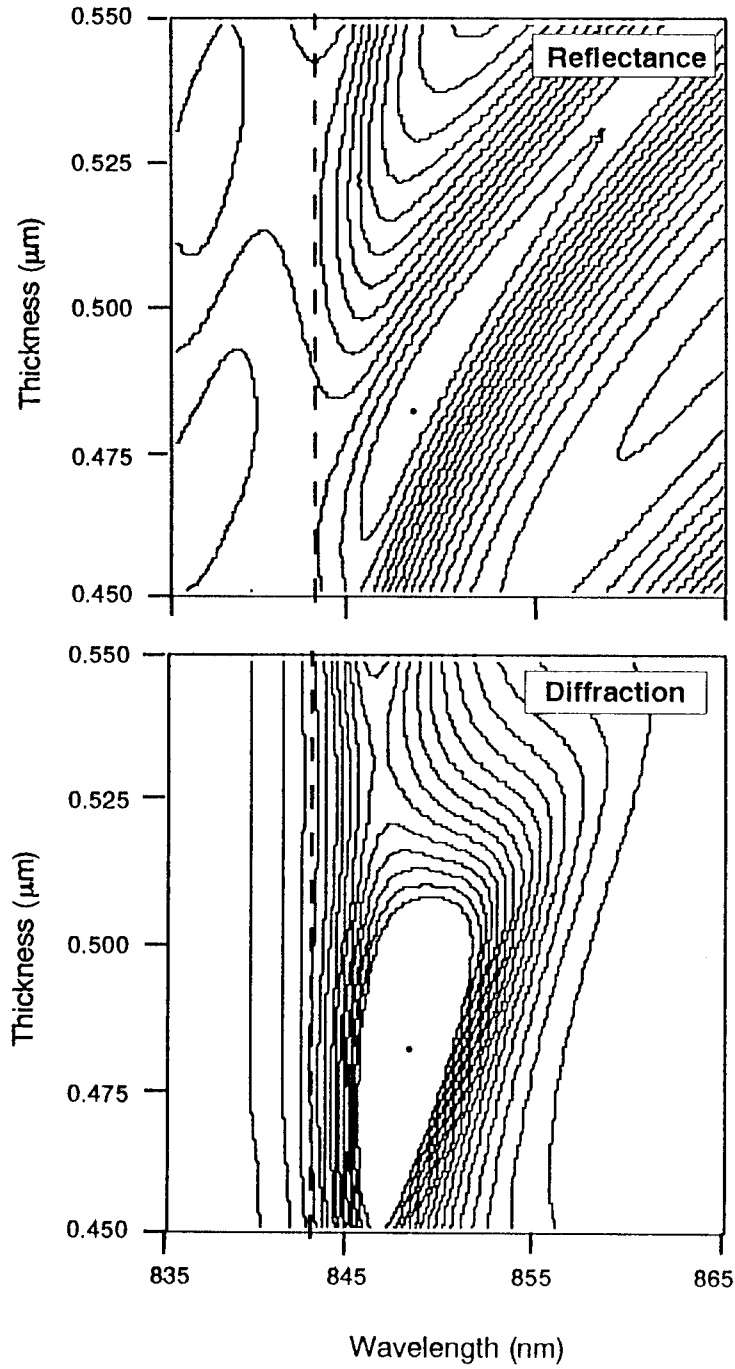


Fig. 4.3 Simulated contours of the reflectance and the reflected diffraction efficiency of a partially asymmetric Fabry Perot. The dashed line marks the exciton transition, and the dot marks the minimum reflectance condition.

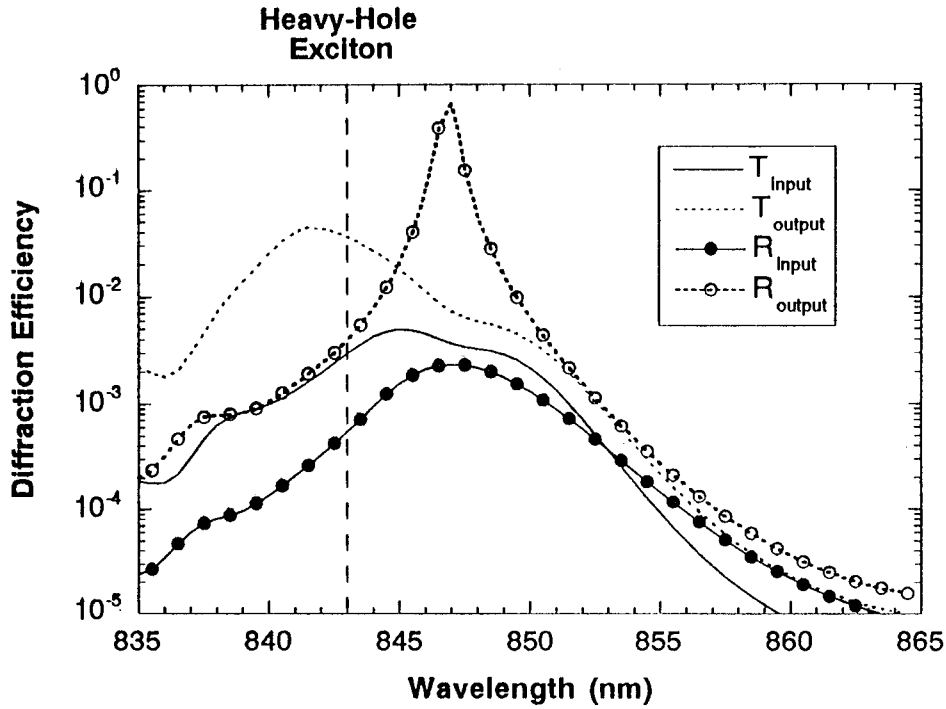


Fig. 4.4 Calculated input and output diffraction efficiencies for transmitted and reflected diffraction orders. The reflected output diffraction efficiency approaches 100%.

The simulation results are shown in Fig. 4.3 for the reflectance and for the input diffraction efficiency as functions of wavelength and device thickness. The device thickness is adjusted in the calculations by assuming that the multiple quantum well layer is sandwiched between two optically inert buffer layers. The Fabry-Perot condition is tuned close to the excitonic transition by adjusting the buffer thickness.

The reflectance in Fig. 4.3a shows the strong dependence of the antireflection condition on device thickness and wavelength. Increasing device thickness pulls the antireflection condition to longer wavelengths. The spot on the figure marks the minimum reflectance condition. The resulting input diffraction efficiency is shown in Fig. 4.3b. It is important to note that the maximum diffraction efficiency *does not* coincide with the exciton transition (shown as the vertical dashed line), but *does* coincide with the optimum antireflection condition. In addition the diffraction efficiency is relatively more weakly dependent on the thickness and wavelength dependence than for

the antireflection condition. The maximum input diffraction efficiency is approximately 0.2%.

The wavelength dependence of the input and output transmitted and reflected diffraction efficiencies are shown in Fig. 4.4. The reflected output diffraction efficiency is largest, with a maximum greater than 50%. This large output diffraction efficiency arises because of the small reflectance at the antireflection condition. The transmitted beam has the largest input diffraction efficiency of 0.4%.

2. Fully Asymmetric Fabry-Perot

Best diffractive performance for a transverse-field photorefractive MQW occurs for the fully asymmetric Fabry-Perot geometry. Calculations for a $\text{Al}_{0.1}\text{Ga}_{0.9}\text{As}/\text{GaAs}$ MQW with a thick layer of gold acting as the back reflector and an field-induced heavy-hole exciton absorption change of $\Delta\alpha_{\text{max}}=2000\text{cm}^{-1}$ yield a maximum input diffraction efficiency of 1.5%.

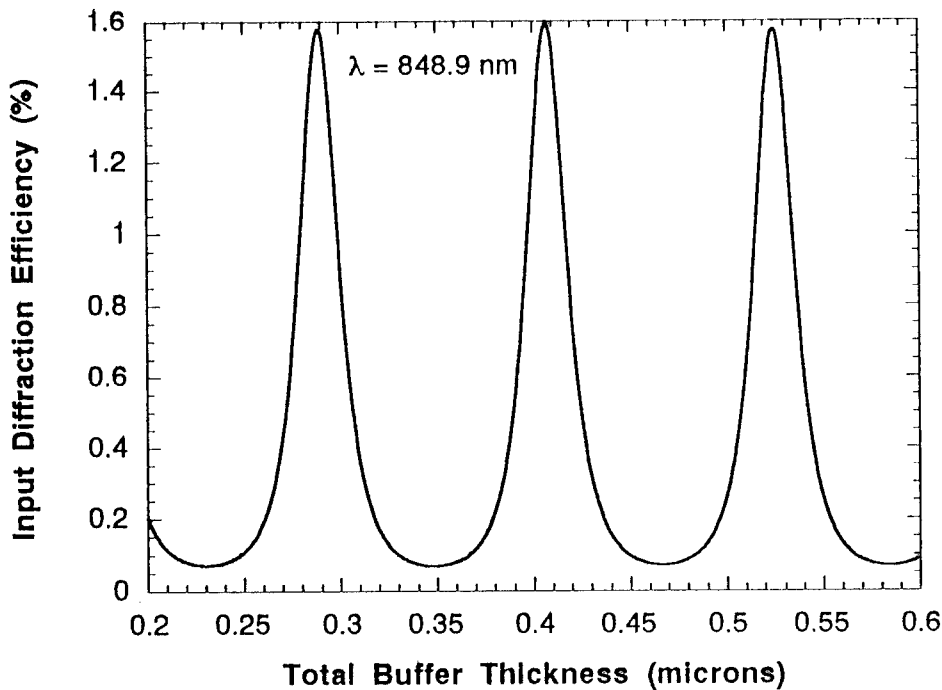


Fig. 4.5 Calculated diffraction efficiency vs. buffer thickness at 848.9 nm for a transverse-field fully asymmetric Fabry-Perot with a $2.0 \mu\text{m}$ thick $\text{Al}_{0.1}\text{Ga}_{0.9}\text{As}/\text{GaAs}$ quantum well region and an applied field of 10 kV/cm .

The effect of the Fabry-Perot fringe placement on the diffraction efficiency is shown in Fig. 4.5. Optimum placement of the Fabry-Perot fringe yields an order of magnitude enhancement in the diffraction efficiency.

B. Longitudinal-Field Geometry

A longitudinal-field geometry, fully asymmetric Fabry-Perot yields the best theoretical input diffraction for a thin film quantum well device [17]. Fig. 4.6 shows the calculated reflectances with and without field for the device thicknesses which yield the maximum and minimum diffraction efficiencies. Maximum diffraction occurs when the Fabry-Perot fringe is placed so that an anti-reflection condition occurs under applied field.

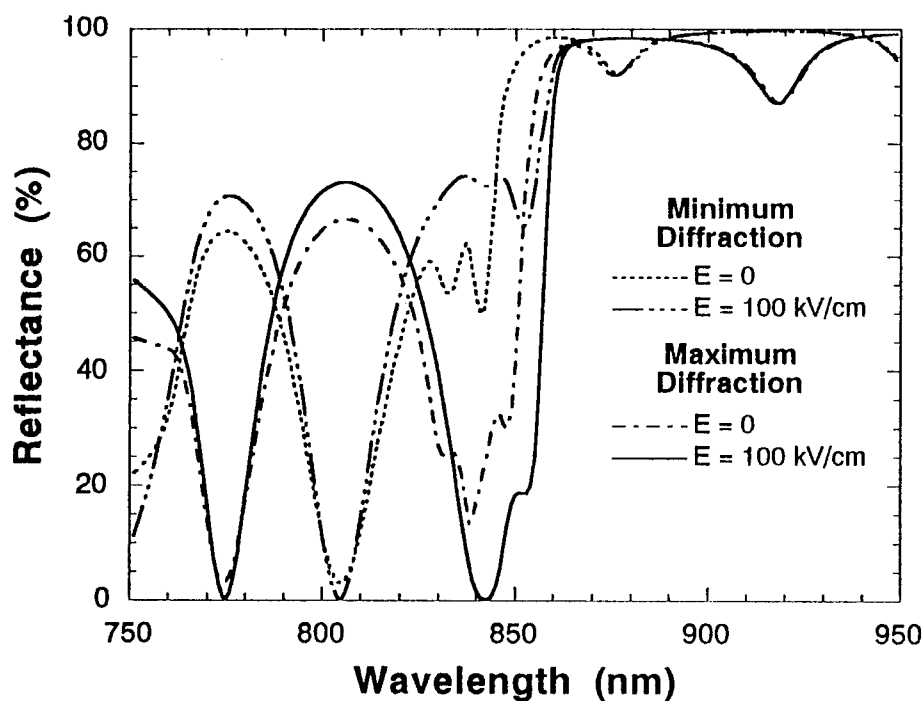


Fig. 4.6 Simulated reflectances with and without field for a longitudinal-field device with a $1.0\ \mu\text{m}$ thick $\text{Al}_{0.3}\text{Ga}_{0.7}\text{As}/\text{GaAs}$ MQW region.

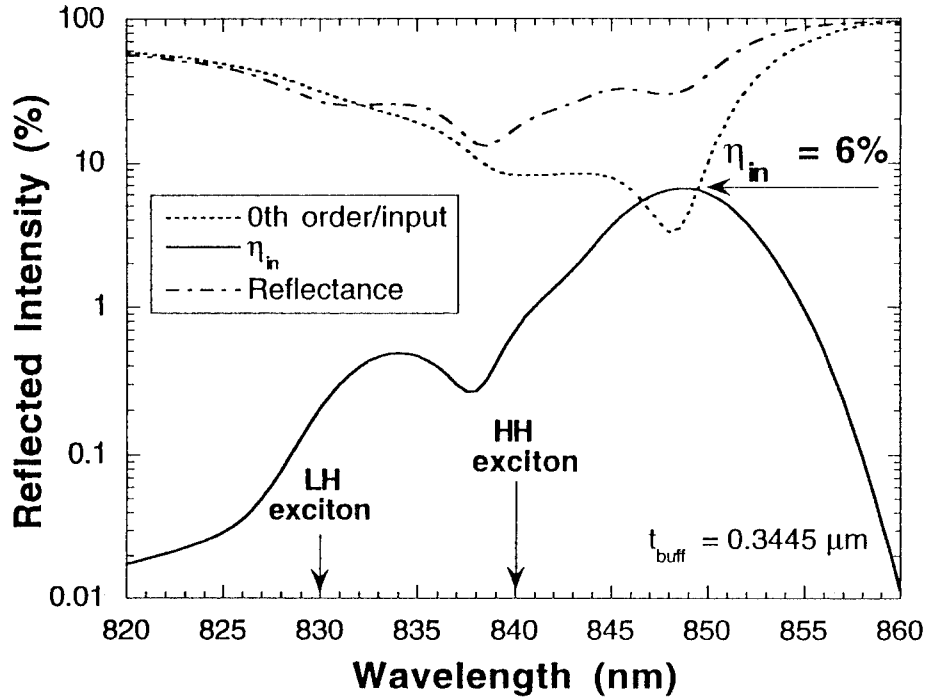


Fig. 4.7. Simulated reflectance, 0-order and first-order diffraction efficiencies for a longitudinal-field ASFP MQW. The buffer thickness of 0.3445 μm was chosen to maximize the first-order diffraction efficiency.

The relative intensities of the reflectance, with no field or grating present, and the 0th and first order diffraction efficiencies are shown in Fig. 4.7. Fabry-Perot phase effects cause the 0th order diffraction to dip below the first order [8]. A maximum input diffraction efficiency of 6.5 % is achieved.

5. Experimental Work

A. Hybrid Device

We first demonstrated a hybrid photorefractive $\text{Al}_{0.1}\text{Ga}_{0.9}\text{As}/\text{GaAs}$ multiple-quantum-well ASFP device with diffraction orders in both transmission and reflection

[18]. The reflection diffraction efficiency was enhanced by a favorable front/back reflectivity ratio for the incident glass-first interface geometry. We demonstrated significant photorefractive diffraction efficiencies that occur simultaneously in transmission and reflection in a quantum-well thin film that was not required to have a perfect anti-reflectance condition. A hybrid device capable of functioning in both transmission and reflection could reduce the number of processing elements needed in an optical computer.

The modulator used in this experiment was grown by molecular beam epitaxy in a Varian Gen-II chamber. A $1\mu\text{m}$ GaAs layer was initially deposited on a n^+ GaAs substrate followed by a 500 \AA AlAs lift-off layer, a 1000 \AA $\text{Al}_{0.2}\text{Ga}_{0.8}\text{As}$ buffer, and a 500 \AA GaAs layer. A 60 period 100 \AA $\text{Al}_{0.1}\text{Ga}_{0.9}\text{As}$ barrier/ 75 \AA GaAs well structure was deposited and followed by a second 1000 \AA $\text{Al}_{0.2}\text{Ga}_{0.8}\text{As}$ buffer and a 50 \AA GaAs cap to prevent oxidation. The structure was proton implanted at 160 keV with a dose of $10^{12}/\text{cm}^2$. The implant introduces deep defects that make the layer semi-insulating and provide traps for photorefractive space-charge gratings [9]. A cold etch ($3\text{H}_3\text{PO}_4:1\text{H}_2\text{O}_2:50\text{H}_2\text{O}$) was used to remove 400 \AA of the top buffer to obtain a Fabry-Perot fringe close to the heavy-hole exciton transition. The modulator surface was protected with wax and liftoff of the thin film was performed by using a highly selective ($>10^8$) 12% HF etch to dissolve the AlAs layer [19]. The sample was then van der Waals bonded to a glass substrate [20]. Two gold contacts were evaporated 1 mm apart on the top surface of the sample to apply a transverse electric field parallel to the quantum-well layers.

Electro-optic characterization was performed with a monochromator and a 600 W Tungsten lamp. A 900 Vp-p modulated DC field (142 Hz) applied parallel to the plane of the quantum-wells was used for all field-dependent incoherent and coherent measurements. Angle-tuning of the incident beam to shift the Fabry-Perot reflectance minimum to the heavy-hole exciton resonance yielded an optimal incident angle of 35° [21]. Reflectance and transmittance at 35° are shown in Fig. 5.1. The minimum reflectance is 10% in this structure when the Fabry-Perot resonance coincides with the exciton transitions. In spite of the moderate modulated contrast that this provides, the reflected diffraction efficiencies are enhanced by an order of magnitude by the phase and amplitude interference effects of the cavity.

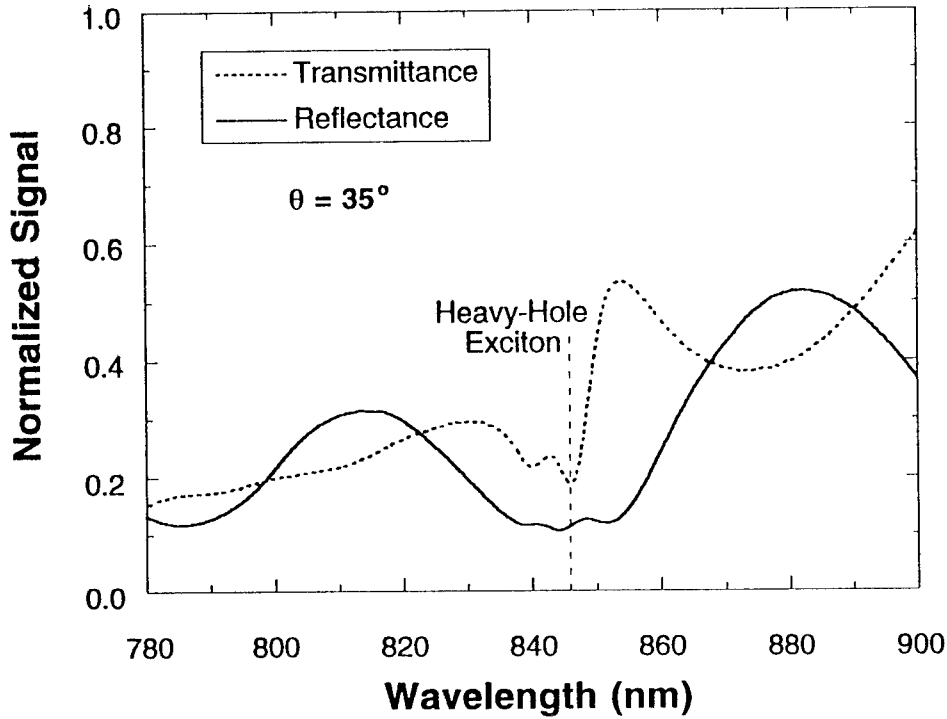


Fig. 5.1 Reflectance and transmittance of the hybrid reflection/transmission ASFP with the light incident on the glass-semiconductor interface at an angle of 35° . The Fabry-Perot fringe is tuned to the exciton transitions.

In non degenerate four-wave mixing experiments, shown in Fig. 5.2, the diffraction grating is written by two HeNe beams [22] incident at equal angles to produce a fringe spacing Λ of $26 \mu\text{m}$. An argon-ion-pumped Ti:Sapphire laser, tunable through the exciton resonance, is used as a probe beam at the optimal incident angle of 35° .

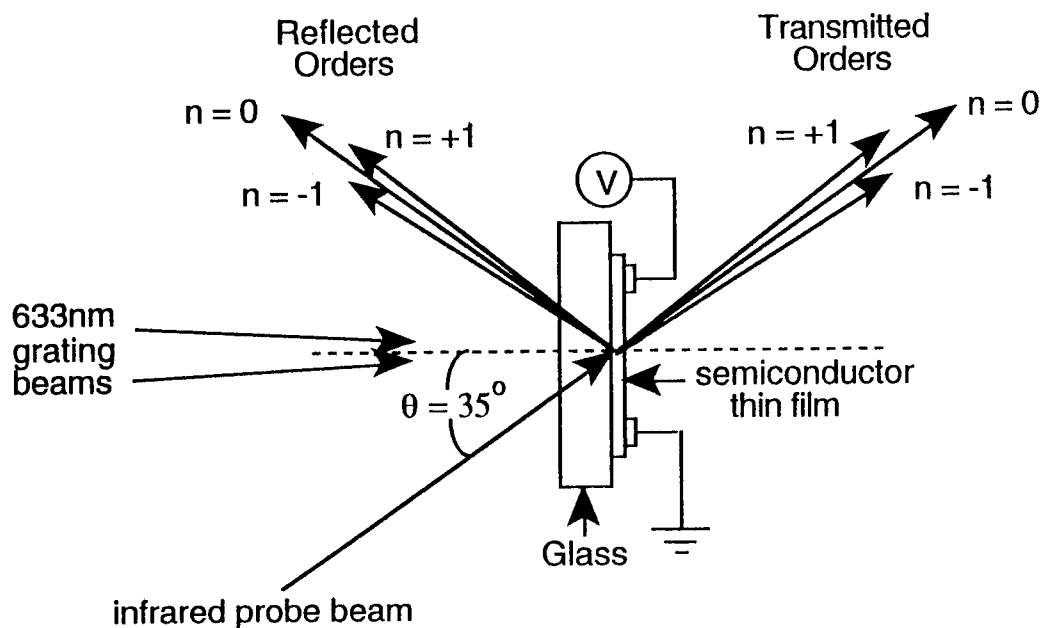


Fig. 5.2 Nondegenerate four-wave mixing geometry with HeNe pump beams writing a photorefractive grating. The infrared probe beam is incident from the glass-first interface and is diffracted in transmission and reflection.

Output diffraction efficiencies for transmission and reflection, when the light is incident on the glass-semiconductor interface, are shown in Fig. 5.3. The output diffraction efficiency, commonly quoted as a figure of merit of these devices, is defined as the ratio of the diffracted signal to the reflected or transmitted signal. Maximum values of 1.3% and 0.7% are obtained in reflection and transmission, respectively. These values are comparable to the 3% value quoted for longitudinal geometry devices [5]. The peak in the transmitted diffraction efficiency occurs near the wavelength of the exciton transition. The peak in the reflected diffraction signal is shifted towards longer wavelengths by the Fabry-Perot resonance at 854 nm.

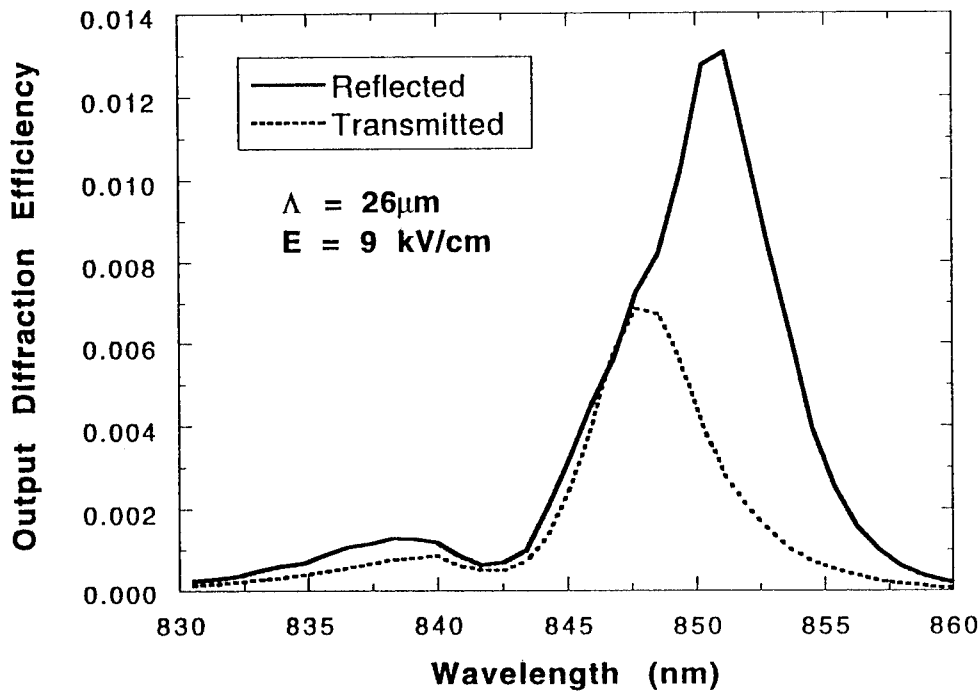


Fig. 5.3 Reflected and transmitted photorefractive output diffraction efficiencies for light incident on the glass-semiconductor interface.

For most optical systems applications it is important to know the through-put of the device, rather than just the output response. For reflective devices in particular, the Fabry Perot interference effects can decrease the reflected signal to zero, yielding an arbitrarily large output diffraction efficiency. The input diffraction efficiency is defined as the ratio of the diffracted signal to the input light signal. The input diffraction efficiency therefore includes all sources of insertion loss and gives the actual conversion efficiency of the device. Input diffraction efficiencies are shown in Fig. 5.4. Maximum values of 0.15% and 0.22% are obtained in reflection and transmission, respectively.

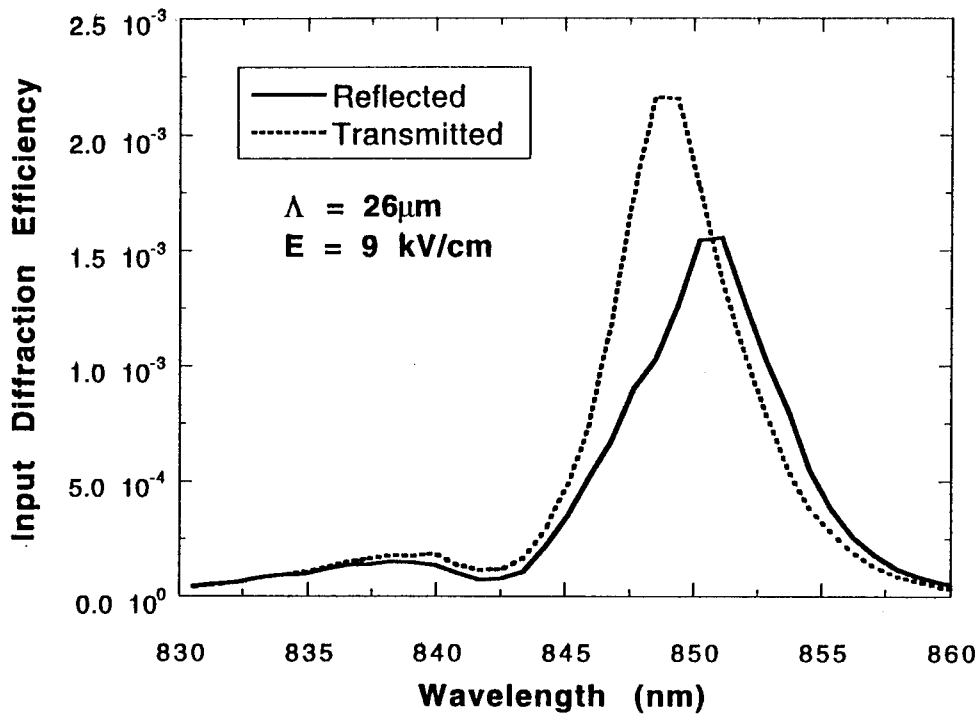


Fig. 5.4 Input diffraction efficiencies for reflection when the light is incident from the glass-semiconductor interface compared with light incident from the semiconductor-air interface. The Fabry-Perot condition in the glass-first case enhances the reflected diffraction efficiency by an order of magnitude.

Reflection input diffraction efficiencies are shown in Fig. 5.5 for light incident from the glass-first interface compared with light incident from the air-first interface. When light is incident on the glass-semiconductor interface, the favorable ratio of reflectance from the front and back interfaces enhances the reflected diffraction efficiencies. On the other hand, when light is incident on the air-semiconductor interface, the front and back reflectivity ratios are unfavorable for interference effects and produce a diffraction efficiency that is an order of magnitude smaller.

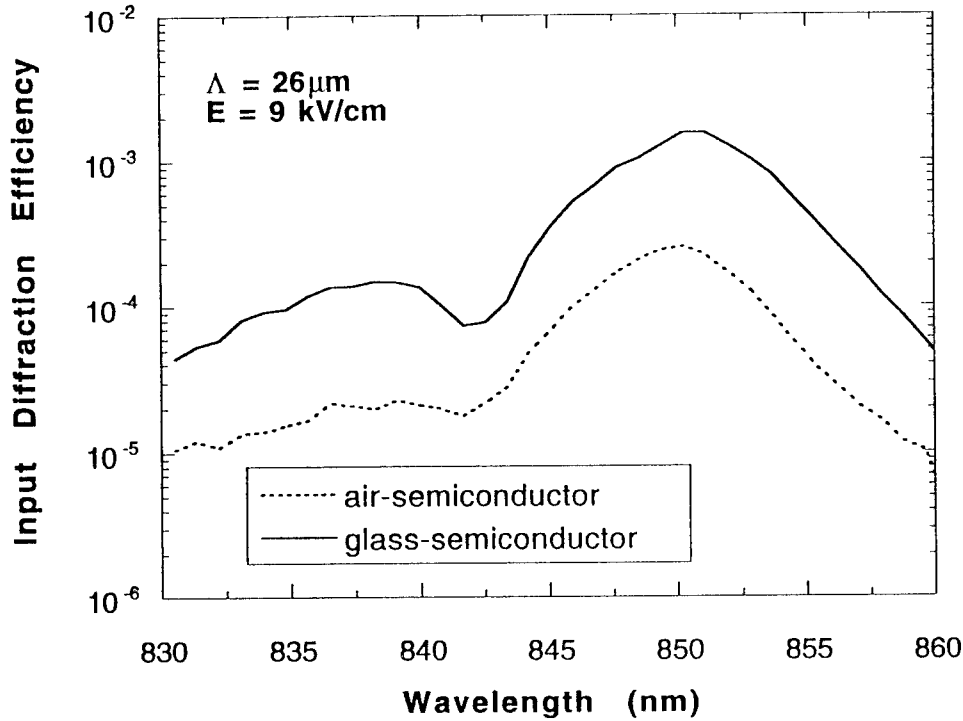


Fig. 5.5 Comparison of glass-first vs. semiconductor-first for the incident interface. The favorable glass-first interface produces an order-of-magnitude improvement in reflected diffraction efficiency.

B. Fully Asymmetric Fabry-Perot

We present an $\text{Al}_{0.1}\text{Ga}_{0.9}\text{As}/\text{GaAs}$ photorefractive quantum-well device with a near optimal input diffraction efficiency of 0.36% and an AlAs/GaAs quantum-well device with an output diffraction efficiency of 200%. Our device operates in the transverse-field geometry utilizing the Franz-Keldysh effect. Output diffraction efficiencies (defined as the ratio of the first-order diffracted intensity to the transmitted or reflected intensity) as large as 200% have been obtained. This efficiency is significantly larger than previous diffraction efficiencies reported for nearly-symmetric Fabry-Pérots operating with transverse fields in transmission and reflection [18] or for non-Fabry-Pérot devices operating with longitudinal fields in transmission [5].

Peak transverse-field photorefractive ASFP performance relies on the optimization of the electroabsorption properties of the quantum-wells, as well as of the Fabry-Pérot. We selected two different structures for our study. In the first structure we optimized the electroabsorption in the transverse-field geometry for standard temperature

growth (STG) quantum-wells. A 10% Al-fraction in the quantum-well barriers optimizes the sensitivity to the applied field for low fields (the largest absorption change per smallest field strength), with better diffractive performance than traditional 30% Al-fraction barriers or GaAs thin films [4]. This device structure yields absorption changes as large as $\Delta\alpha = 3000 \text{ cm}^{-1}$ for applied fields as small as 8 kV/cm. The design of the STG $\text{Al}_{0.1}\text{Ga}_{0.9}\text{As}/\text{GaAs}$ ASFP was optimized using computer simulations [17]. A 1.5 micron thick $\text{Al}_{0.1}\text{Ga}_{0.9}\text{As}/\text{GaAs}$ MQW region was chosen to provide the absorption necessary to balance the asymmetric front ($R = 31\%$) and back ($R > 95\%$) mirror reflectivities. The second structure we studied was a low temperature growth (LTG) AlAs barrier MQW. The advantages of LTG AlAs/GaAs quantum-wells include higher breakdown field and lower leakage currents. LTG AlAs/GaAs is automatically semi-insulating when annealed [23]. AlAs barriers yield higher quantum confinement and allow the device to perform at higher fields than $\text{Al}_{0.1}\text{Ga}_{0.9}\text{As}$ barriers.

The photorefractive ASFP devices were grown in a Varian Gen-II molecular beam epitaxy chamber on a GaAs substrate. The STG 10% Al barrier structure, grown at 600°C , consists of a $\text{Al}_{0.5}\text{Ga}_{0.5}\text{As}$ stop-etch layer beneath a $1.5 \mu\text{m}$ 100\AA $\text{Al}_{0.1}\text{Ga}_{0.9}\text{As}/75\text{\AA}$ GaAs MQW region sandwiched between $\text{Al}_{0.1}\text{Ga}_{0.9}\text{As}$ buffer layers used to control the total device thickness. Deep defects were introduced by proton implantation at a double dose of $10^{12}/\text{cm}^2$ at 160 keV and $5 \times 10^{11}/\text{cm}^2$ at 80 keV to make the device semi-insulating throughout the MQW region. The defects provide traps for photorefractive space-charge gratings. This device design incorporated all important design characteristics for best input diffraction efficiency performance, including optimum barrier Al-fraction, high optical surface quality, sufficient absorption to balance the ASFP, and a favorable Fabry-Pérot fringe placement. The LTG AlAs barrier structure consists of a $2.0 \mu\text{m}$ 20\AA AlAs/ 100\AA GaAs MQW region sandwiched between $\text{Al}_{0.1}\text{Ga}_{0.9}\text{As}$ buffers on a $\text{Al}_{0.5}\text{Ga}_{0.5}\text{As}$ stop-etch layer. The stop etch layer was grown at 600°C while the MQW region and the buffers were grown at 320°C . Annealing at 600°C for 30 seconds made the material semi-insulating by the formation of As precipitates. The As clusters deplete free carriers from the surrounding material yielding high resistivity. The top surfaces of both structures were coated at Thin Film Lab with a dielectric mirror specially designed for use on semi-insulating material with $>95\%$ reflectivity in the 800 nm-900 nm wavelength range centered on the exciton resonances. A room temperature etch in $1\text{NH}_4\text{OH}:19\text{H}_2\text{O}_2$ removed the substrate and HF acid was used to remove any remaining stop-etch material. The HF acid soak also maximizes the chance of a good Fabry-Pérot condition because the HF etch rate changes by many orders

of magnitude as the aluminum fraction is reduced below 40% [19]. The high-reflectivity rear-reflector and careful control of the overall thickness of the device and optical quality of the front and back surfaces increase the chance of a strong and favorably-placed Fabry-Pérot resonance. A cold etch ($3\text{H}_3\text{PO}_4:1\text{H}_2\text{O}_2:50\text{H}_2\text{O}$) can also be used to remove some of the $\text{Al}_{0.1}\text{Ga}_{0.9}\text{As}$ buffer to tune a Fabry-Pérot fringe to an energy just below that of the heavy hole exciton resonance. After etching, two gold contacts were deposited 1 mm apart on the sample.

The reflectance and differential reflectance for the STG 10% Al barrier device were measured with an 800 V modulated DC field (142 Hz) applied parallel to the quantum-wells. The reflectance and differential reflectance are shown in Fig. 5.6.

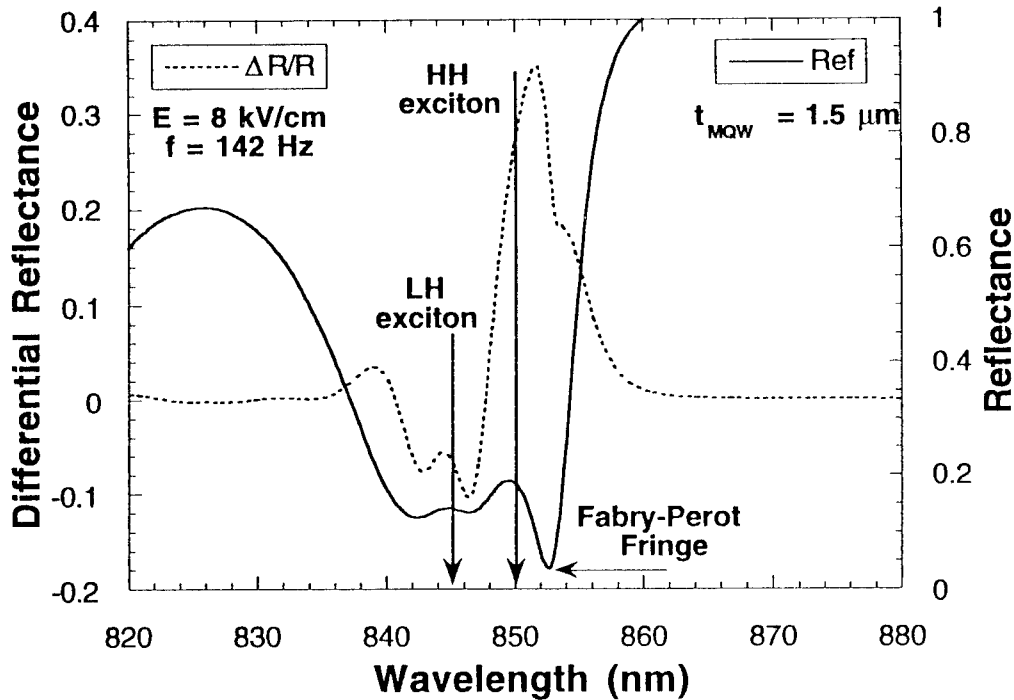


Fig. 5.6 Zero-field reflectance and differential reflectance of the 10% Al barrier device for an 8 kV/cm transverse applied field. The moderate contrast ratio of 35% results from averaging the reflectance over the entire area of the 1 mm x 2.5 mm device. The light- and heavy-hole exciton transition wavelengths are shown for comparison.

The Fabry-Pérot minimum reflectance is approximately 4%, averaged over the broad area of the device. The reflection minimum at 852.5 nm lies at the low-energy side of the

heavy hole exciton resonance that occurs at 850 nm. The maximum differential reflectance of 35% occurs near the Fabry-Pérot resonance due to the field-induced absorption and index changes. It is important to emphasize that photorefractive quantum-well devices are broad-area devices with active operation areas as large as 1 cm^2 . These devices therefore have more stringent requirements for uniform device thickness over broad areas. As a result, it is difficult to obtain exact Fabry-Pérot cavity resonances over the entire active area, which leads to only moderate contrast ratios of 35% in our devices, averaged over the large device active area.

Non-degenerate four-wave mixing [2] experiments were conducted using two 690 nm diode laser beams to write a diffraction grating with a fringe spacing of $25 \text{ }\mu\text{m}$. A tunable Ti:Sapphire laser was used as a probe beam at an incident angle of 15 degrees with the use of an aperture so all the probe light fell on the device area and did not overlap the gold contacts.

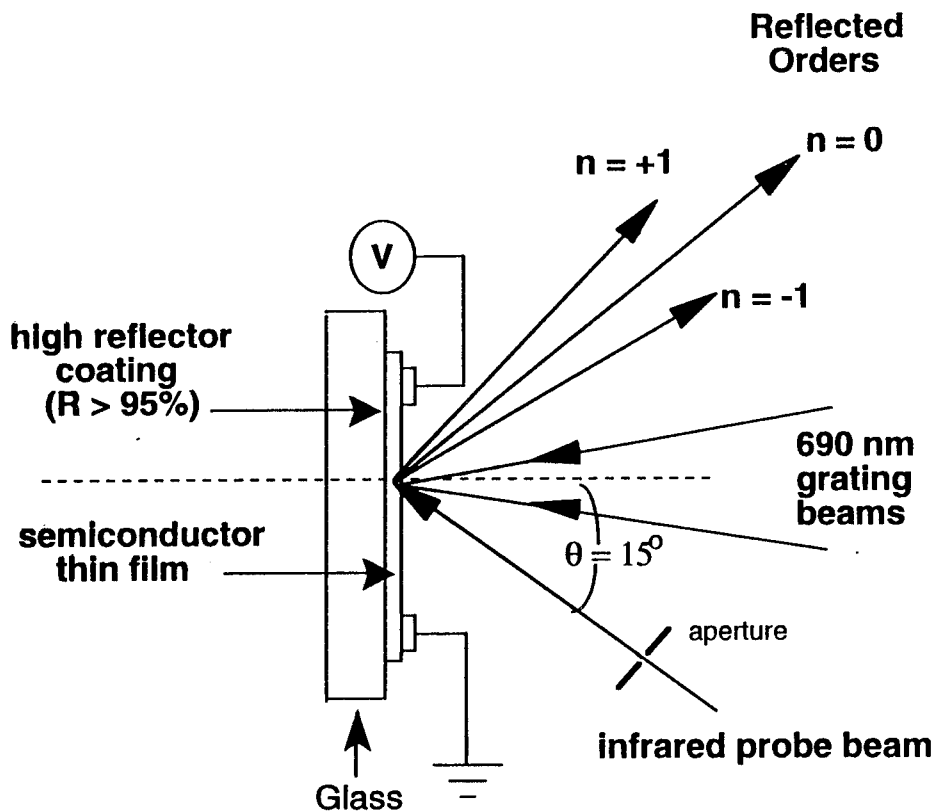


Fig. 5.7 Experimental geometry for four-wave mixing in reflection from a fully asymmetric Fabry-Pérot.

The diffraction efficiency is a strong function of the overall intensity as well as of the intensity ratio of the grating and probe beams. For the 10% Al barrier device a probe intensity of $250 \mu\text{W}/\text{cm}^2$ and an approximate grating beam intensity of $4.75 \text{ mW}/\text{cm}^2$ were used. Approximate probe and grating beam intensities of $5 \text{ mW}/\text{cm}^2$ and $150 \text{ mW}/\text{cm}^2$, respectively, were used for the two LTG devices. The zero- field reflected and first -order diffraction beams are detected with silicon photo-diode detectors through 750 nm long-pass filters. The zero-order beam is mechanically chopped at 142 Hz and detected with a lock-in amplifier while the first-order diffraction is detected by modulating the electric field at 142 Hz.

The output diffraction efficiency is defined as the ratio of the diffracted intensity to the transmitted or reflected intensity. In previous reports of photorefractive quantum-well performance the output diffraction efficiency has been quoted exclusively. However, for many optical systems it is important to include insertion-loss and device absorption in the diffracted figure-of-merit. The input diffraction efficiency, defined as the ratio of the diffracted beam to the input beam, is therefore often a more appropriate parameter. The output diffraction efficiencies and the corresponding peak input diffraction efficiencies of the two photorefractive ASFP structures are shown in Fig. 5.8 as functions of wavelength. The diffraction peak of the 10% Al barrier device is shifted towards the Fabry-Pérot fringe at 852.5 nm. An output diffraction efficiency as large as 15% has been obtained in this device. The diffraction efficiencies from two of the LTG devices are also shown. These two LTG devices differ from each other only in their buffer thickness, and therefore in their Fabry-Pérot fringe position. The output diffraction efficiency reaches nearly 200% for a well-balanced cavity in LTG AlAs barrier device #2. A different buffer thickness reduces the output diffraction efficiency to 50% in LTG AlAs barrier device #1. The corresponding input diffraction efficiency is larger in LTG device #1 due to a Fabry-Pérot resonance closer to the heavy-hole exciton at 844 nm. No significant diffraction is seen at the exciton resonances in these devices. A thicker MQW region and the additional background absorption from the incorporated arsenic precipitates [24] lower the input diffraction efficiencies for the LTG devices compared to the STG 10% Al barrier device.

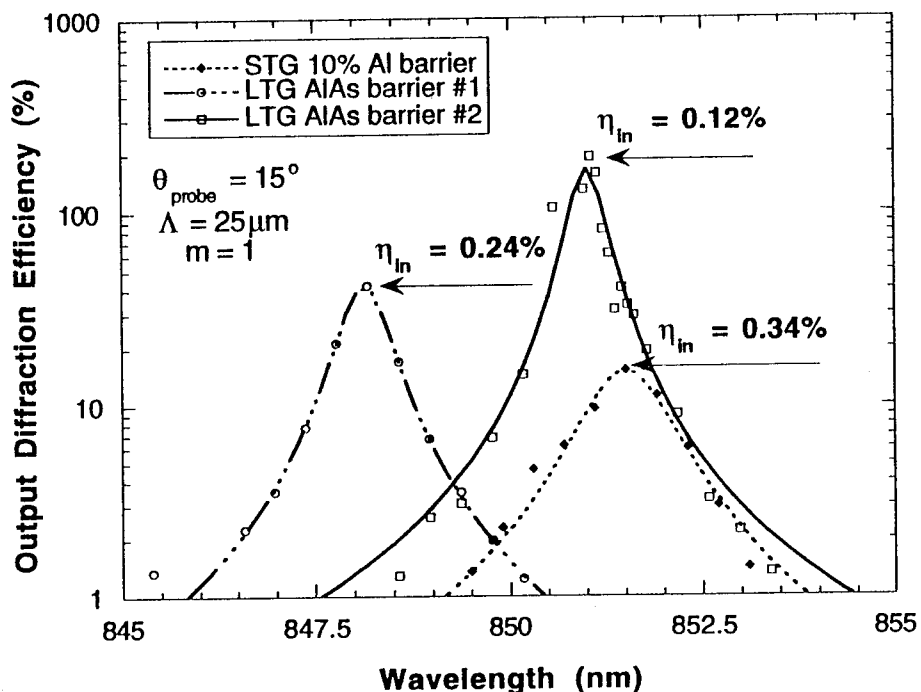


Fig. 5.8 Output and peak input diffraction efficiencies for the MQW ASFPs. The 10% Al barrier device was tested with a modulated DC field of 8 kV/cm at 142 Hz and an approximate total light intensity of 5.0 mW/cm². The two LTG AlAs barrier devices were tested with a modulated DC field of 15 kV/cm at 142 Hz and an approximate total light intensity of 155 mW/cm².

Fig. 5.9 shows the input diffraction efficiency (including all insertion-loss and absorption) of the STG 10% Al barrier device superimposed on the differential reflectance. The diffraction maximum occurs between the wavelength of the heavy-hole exciton and the wavelength of the Fabry-Pérot fringe. The maximum input diffraction efficiency from this device is 0.36%. Best transverse-field photorefractive ASFP performance is predicted from computer simulations [8] to yield an input diffraction efficiency of approximately 1%, assuming perfect device growth and fabrication. Therefore, the device demonstrated here has close to the theoretical best performance for this device geometry. Variations in device thickness across the broad area can easily account for the remaining inefficiency. It is important to emphasize that the Fabry-Pérot resonance significantly enhances the diffraction even at the wavelength of the heavy-hole exciton transition. The Fabry-Pérot provides nearly an order of magnitude improvement

in the maximum input diffraction efficiency over non-Fabry-Perot photorefractive quantum well structures.

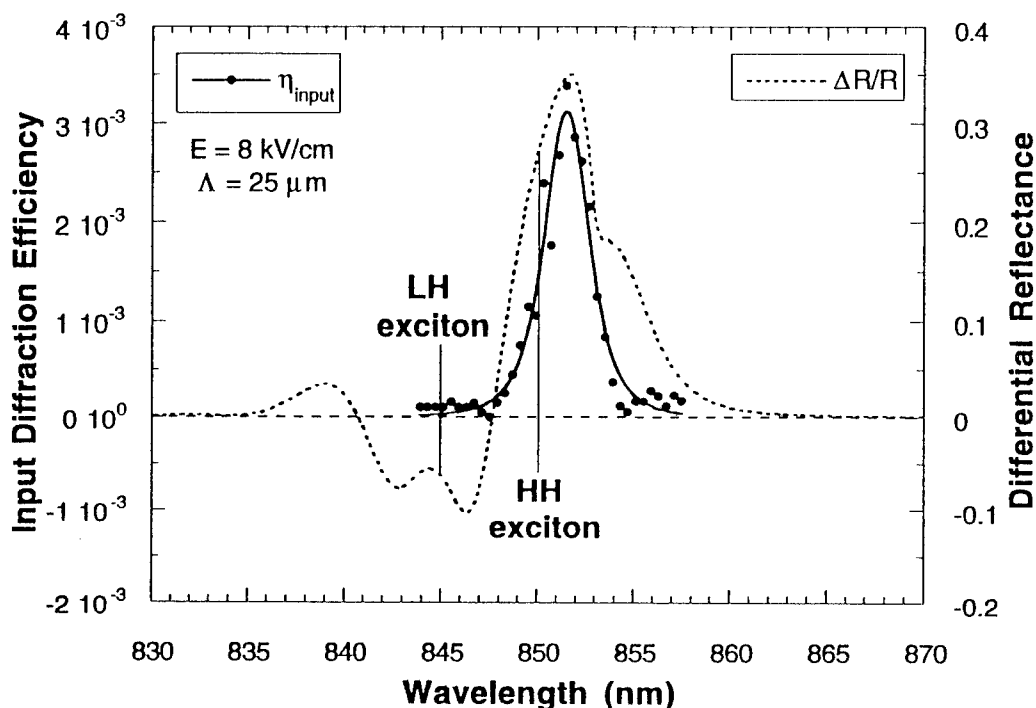


Fig. 5.9 Input diffraction efficiency, η_{in} , and differential reflectance of the STG 10% Al barrier device demonstrating the influence of the Fabry-Pérot resonance at 852.5nm on the diffraction. A near optimal η_{in} of 0.36% is achieved for this device geometry.

6. Discussion and Future

In conclusion, we have demonstrated a hybrid photorefractive quantum-well structure that uses Fabry-Perot interference effects to enhance reflected diffraction efficiencies. We obtain output diffraction efficiencies of 1.3% in reflection and 0.7% in transmission, corresponding to input diffraction efficiencies of 0.15% in reflection and 0.22% in transmission. We have also demonstrated a STG 10% Al barrier transverse-field photorefractive MQW ASFP with a near-optimum input diffraction efficiency of 0.36% and an output diffraction efficiency of 15% and an LTG AlAs barrier MQW ASFP with an output diffraction efficiency of nearly 200%. The observed diffraction is significantly enhanced by the Fabry-Pérot resonance.

Further performance optimization in photorefractive quantum-wells may be achieved in longitudinal field geometries using the quantum-confined Stark effect. Computer simulations predict a maximum input diffraction efficiency of 6.5% for the longitudinal-field geometry [17].

7. Bibliography

- ¹S. C. W. Hyde, N. P. Barry, R. Jones, J. C. Dainty, P. M. W. French, M. B. Klein and B. A. Wechsler, *Opt. Lett.* **20**, 1331 (1995)
- ²Q. N. Wang, R. M. Brubaker, D. D. Nolte and M. R. Melloch, *J. Opt. Soc. Am. B* **9**, 1626 (1992)
- ³D. D. Nolte and M. R. Melloch, *Mater. Res. Bull.* **19**, 44 (1994)
- ⁴D. D. Nolte and M. R. Melloch, in *Photorefractive Quantum Wells and Thin Films* D. D. Nolte, ed., (Kluwer Academic Publishers, Dordrecht, 1995)
- ⁵A. Partovi, A. M. Glass, D. H. Olson, G. J. Zydzik, H. M. O'Bryan, T. H. Chiu and W. H. Knox, *Appl. Phys. Lett.* **62**, 464 (1993)
- ⁶D. S. Gerber, R. Droopad and G. N. Maracas, *IEEE Phot. Tech. Lett.* **5**, 55 (1993)
- ⁷B. Pezeshki, G. A. Williams and J. S. Harris Jr., *Appl. Phys. Lett.* **60**, 1061 (1992)
- ⁸D. D. Nolte, *Opt. Lett.* **19**, 819 (1994)
- ⁹D. D. Nolte, D. H. Olson, G. E. Doran, W. H. Knox and A. M. Glass, *J. Opt. Soc. Am. B* **7**, 2217 (1990)
- ¹⁰R. Yan, R. J. Simes and L. A. Coldren, *IEEE J. Quant. Electron.* **25**, 2272 (1989)
- ¹¹K.-K. Law, R. H. Yan, L. A. Coldren and J. L. Merz, *Appl. Phys. Lett.* **57**, 1345 (1990)
- ¹²M. F. Krol, T. Ohtsuki, G. Khitrova, R. K. Boncek, B. P. McGinnis, H. M. Gibbs and N. Peyghambarian, *Appl. Phys. Lett.* **62**, 1550 (1993)
- ¹³T. H. Wood, *J. Lightwave Tech.* **6**, 743 (1988)
- ¹⁴O. S. Heavens, *Optical Properties of Thin Films* (New York, Dover, 1991)
- ¹⁵D. S. Chemla, D. A. B. Miller, P. W. Smith, A. C. Gossard and W. Wiegmann, *IEEE J. Quant. Electron.* **QE-20**, 265 (1984)
- ¹⁶D. A. B. Miller, D. S. Chemla, T. C. Damen, A. C. Gossard, W. Wiegmann, T. H. Wood and C. A. Burrus, *Phys. Rev. B* **32**, 1043 (1985)
- ¹⁷D. D. Nolte and K. M. Kwolek, *Opt. Comm.* **115**, 606 (1995)
- ¹⁸K. M. Kwolek, M. R. Melloch and D. D. Nolte, *Appl. Phys. Lett.* **65**, 385 (1994)
- ¹⁹E. Yablonovitch, T. Gmitter, J. P. Harbison and R. Bhat, *Appl. Phys. Lett.* **51**, 2222 (1987)
- ²⁰E. Yablonovitch, D. M. Hwang, T. J. Gmitter, L. T. Florez and J. P. Harbison, *Appl. Phys. Lett.* **56**, 2419 (1990)
- ²¹P. Tayebati, *Appl. Phys. Lett.* **63**, 2878 (1993)
- ²²D. D. Nolte, Q. N. Wang and M. R. Melloch, *Appl. Phys. Lett.* **58**, 2067 (1991)

²³M. R. Melloch, J. M. Woodall, E. S. Harmon, D. D. Nolte, N. Otsuka, F. H. Pollak, R. M. Feenstra and M. A. Lutz, *Annual Review of Materials Science* (Palo Alto, CA, Annual Reviews, 1995)

²⁴D. D. Nolte, *J. Appl. Phys.* **76**, 3740 (1994)

MISSION
OF
ROME LABORATORY

Mission. The mission of Rome Laboratory is to advance the science and technologies of command, control, communications and intelligence and to transition them into systems to meet customer needs. To achieve this, Rome Lab:

- a. Conducts vigorous research, development and test programs in all applicable technologies;
- b. Transitions technology to current and future systems to improve operational capability, readiness, and supportability;
- c. Provides a full range of technical support to Air Force Materiel Command product centers and other Air Force organizations;
- d. Promotes transfer of technology to the private sector;
- e. Maintains leading edge technological expertise in the areas of surveillance, communications, command and control, intelligence, reliability science, electro-magnetic technology, photonics, signal processing, and computational science.

The thrust areas of technical competence include: Surveillance, Communications, Command and Control, Intelligence, Signal Processing, Computer Science and Technology, Electromagnetic Technology, Photonics and Reliability Sciences.